

# Microkinetic evaluation of normal and inverse kinetic isotope effects during methane steam reforming to synthesis gas over a Ni/NiAl<sub>2</sub>O<sub>4</sub> model catalyst

C. Sprung<sup>a</sup>, P.N. Kechagiopoulos<sup>b</sup>, J.W. Thybaut<sup>b,\*</sup>, B. Arstad<sup>c</sup>, U. Olsbye<sup>a</sup>, G.B. Marin<sup>b</sup>

<sup>a</sup> University of Oslo, Department of Chemistry, P.O. Box 1033, NO-0315 Oslo, Norway

<sup>b</sup> Ghent University, Laboratory for Chemical Technology, Technologiepark 914, B-9052 Ghent, Belgium

<sup>c</sup> SINTEF Materials and Chemistry, Pb. 124, NO-0314 Oslo, Norway

## ARTICLE INFO

### Article history:

Received 6 June 2014

Received in revised form 8 October 2014

Accepted 13 October 2014

Available online 23 December 2014

### Keywords:

Microkinetic modelling  
Methane steam reforming  
Kinetic isotope effect  
Reaction pathway  
Partial equilibrium

## ABSTRACT

A microkinetic model was developed and applied to simulate an extensive experimental dataset on methane steam reforming. The data set consisted of 537 data points, and was collected over a Ni/NiAl<sub>2</sub>O<sub>4</sub> catalyst at 843, 858, and 873 K in a wide steam-to-carbon ratio range between 0.2 and 7.1. A microkinetic engine modeling tool was applied for the construction and parameter estimation of an elementary step network consisting of 12 reversible reactions. Specific reaction pathways were implemented for the formation of CO and CO<sub>2</sub>, respectively. The model qualitatively if not quantitatively explains inverse and normal isotope effects experimentally observed at low and high S/C ratios, respectively, and is thermodynamically consistent. A combination of the approach to partial equilibrium (i.e. whether the elementary step proceeds forward or backward) and net rate (i.e. the difference between forward and backward reaction rate) provides novel insight into the oxidation mechanism of CH<sub>x</sub> and CH<sub>x</sub>O surface species.

© 2014 Elsevier B.V. All rights reserved.

## 1. Introduction

Natural gas is an important source in the global energy supply chain [1]. Methane, the major component in natural gas, is furthermore, utilised for the production of valuable chemicals via its conversion to synthesis gas (also denoted as syngas, a CO/H<sub>2</sub> mixture) [2], which is then further processed. The most important products out of natural gas are methanol and pure hydrogen, with ammonia representing a further important downstream derivative [3].

Methane steam reforming (MSR) over nickel catalysts is a major process for syngas production, and especially pure hydrogen production [2,3]. Early investigations on the kinetics of the MSR process were based on simple kinetic models. Gaseous molecules were assumed to react with adsorbed surface species upon collision [4–6]. Further developments incorporated the adsorption of all reactants and products [7,8]. Empirical rate equations were derived and gave a satisfactory description of the investigated experimental conditions [9].

Additionally, the concentration of species on the catalyst surface was incorporated in the rate expression [10–12], and its physical

meaning was validated. Adsorption coefficients and corresponding enthalpies were estimated and compared to values derived from experimental methods. Such Langmuir–Hinshelwood approaches were based on elementary step models, in which one or several kinetically relevant steps are assumed. The respective rate expressions were derived accordingly. Due to the presence of reactant partial pressures in the numerator and, also, the denominator, the dependence of the reaction rate on a specific reactant partial pressure may be non-monotonic. These rate expressions [5,6,10–13] describe experimental observations in a broader range of operating conditions [14], and are, therefore, preferred in industrial applications.

The kinetic picture of methane steam reforming taken from the reported work in the last two paragraphs may be divided into two main categories, i.e., one where the methane adsorption [7,9,13,15], and a second one where an oxidation reaction on the surface [5,10–14,16], respectively, was assumed to be rate determining. The former statement was supported from isotopic labelling investigation on Ni/MgO catalysts, where methane adsorption was found to be irreversible [9]. In contrast to that, pulse experiments under vacuum conditions for nickel on different supports could show the fast adsorption of methane [17,18]. Investigations reported for a Ni/Al<sub>2</sub>O<sub>3</sub> catalyst show that isotope effects depend on the reaction conditions [19].

\* Corresponding author. Tel.: +32 93311752; fax: +32 93311759.

Further insight into mechanistic features was provided by microkinetic modelling and DFT calculations. The former approaches do assume an elementary step model, however, without considering a rate-determining step. Both experimental and theoretical data are accounted for [20–23]. The estimated activation energies and simulated concentrations of reaction intermediates offer valuable information about possible reaction pathways and the reaction rates. Kinetically relevant elementary steps as identified in literature models were the methane adsorption and dehydrogenation [20,23,24], and the C–O and OC–O bond formation [20]. Thus, it is possible and even likely that more than one step is significantly affecting the overall rate, when the experimental observations have been performed in a broad range of operating conditions. Such microkinetic models simulate the experimental data rather well in terms of reactant conversions and product selectivity [20,21,23–26].

More details on reaction pathways can be achieved from DFT calculations. Thermochemical characteristics of the surface intermediates were determined and, hence, allowed interpretations based on the free energy, which incorporates entropic effects. In accord with the categorisation mentioned above, CH<sub>4</sub> dissociation [24,27] and an oxidation reaction of C\* [27,28], and CH\* [24,28], respectively, may serve as a rate-determining step. It has been found that the temperature has a significant effect on which step could eventually be rate-determining [27,28], and which intermediate is part of the main reaction pathway for the oxidation reaction (C\* or CH\*) [28]. In a site dependent investigation by Blaylock et al. [28] generally higher binding and adsorption energies were predicted on the step edges Ni(2 1 1), in comparison to the Ni(1 1 1) and Ni(1 0 0) facets. Hence, the reaction pathways differ for various sites on Ni surfaces. Even though DFT calculations give valuable insight into the mechanism, a main challenge remains to describe experimental data quantitatively.

In this investigation we employ a microkinetic modelling approach to describe the experimental data provided in Sprung et al. [29]. Both reactants were found to affect the methane conversion rate [29,30]. The partial reaction orders of steam and methane varied from zero, or even negative for steam, to one, depending on the S/C applied. Based on the partial reaction orders of the reactants, two kinetic regimes were distinguished. At low S/C the kinetics were determined by high steam and low methane partial reaction orders, whereas the situation was inverse at high S/C. Switch experiments under steady state conditions between CH<sub>4</sub> and CD<sub>4</sub> feed revealed kinetic isotope effects (KIE – ratio of methane conversion at CH<sub>4</sub>/H<sub>2</sub>O to CD<sub>4</sub>/H<sub>2</sub>O feed, i.e.,  $x_H/x_D$ ). This effect was inverse (i.e., <1) at low S/C, and normal (i.e., >1) for experiments under high S/C conditions.

The isotope effect caused by the hydrogen isotopes is the most pronounced due to their relative mass difference (deuterium (D), and tritium (T) are two-, and threefold, respectively, the mass of protium (H)). Such a mass difference has remarkable influence on the chemical bond between two atoms, especially their vibrational levels. Details on the origin of isotope effects are found in the literature in this field [31,32]. The cleavage of a C–H requires less energy compared to a C–D bond. The isotope effect in that case is *normal*, i.e., >1 due to a faster reaction for C–H than C–D bond cleavage [31,32]. An *inverse* isotope effect is, in contrast to the *normal* effect, not caused by a bond cleavage process, and is in general of minor magnitude compared to the former. An overview on the possible origins of an *inverse* isotope effect with focus on methane steam reforming was given in Ref. [29], and shall not be repeated here. It was concluded that the origin is most likely a hybridisation change towards more p-like orbitals (i.e.,  $sp^2 \rightarrow sp^3$ , for which an isotope effect of 0.8–0.9 is expected [32]). Hence, the C–H/C–D bond has to stay intact at the carbon atom, which takes part in the reaction.

In conclusion, the occurrence of both an inverse and a normal isotope effect at low and high S/C, respectively, suggests that two different reaction pathways are kinetically relevant: i.e., one where the C–H bond stays intact and a second one where this bond is cleaved.

Isotope effects were so far introduced in connection to kinetics, i.e., in the way the experiments have been carried out [29]. The thermodynamic isotope effect (TIE) is defined as the ratio of equilibrium coefficients, i.e.,  $K_H/K_D$  [31,33]. Kiperman proposed a concept in which an observed isotope effect is composed of both a kinetic and a thermodynamic isotope effect [34]. An overall normal TIE was observed for methane steam reforming under thermodynamic equilibrium conditions, however an inverse isotope effect on the methane conversion was simulated for low S/C ratios [35]. We want to widen the field of view in this topic, and also consider equilibrium/thermodynamic isotope effects for surface reactions in partial equilibrium.

In summary the two kinetic regimes distinguished by the categorised partial reaction orders of the reactants [29,30] and the observed kinetic isotope effects [29] discard the assumption of a single reaction step determining the rate of the overall reaction in the investigated S/C range. A microkinetic modelling approach was, therefore, considered. The mechanistic features of the model established by Xu and Froment [11] were used as a basis for the developed microkinetic model, however in contrast to the approach of the latter authors, no rate-determining step was assumed in the current work. Hence, it was possible to identify and evaluate all kinetically relevant reaction steps at the wide range of studied conditions. The final elementary step model with 12 reversible reactions was developed on the basis of the experimental observations reported in [29,30].

## 2. Catalyst and experimental procedure

A brief summary of the catalyst synthesis and experimental procedure will be given here. Further details on catalyst synthesis, characterisation, the experimental equipment and the catalytic testing procedure are reported by Sprung et al. [29,30,35].

The catalyst was a 2 wt% NiO/NiAl<sub>2</sub>O<sub>4</sub>. A water/i-propanol solution of nickel nitrate and aluminum nitrate was dried and the solid precursor calcined at 1473 K in static air. The catalyst, diluted with  $\alpha$ -Al<sub>2</sub>O<sub>3</sub> (1:50, 250–420  $\mu$ m, total catalyst bed mass 500 mg), was placed inside an alumina fixed bed tubular reactor. Gas flows were controlled by an array of mass flow controllers. Steam was provided by a two stage steam generator set-up, where an Ar gas stream was flushed through water at elevated temperatures. Two MicroGC's (Agilent 3000) analyzed simultaneously reactant and product gases.

After activation in 10 vol% H<sub>2</sub>/Ar at 873 K the catalyst was stabilized at 873 K and reference conditions (6.3% CH<sub>4</sub>, 12.3% H<sub>2</sub>O in Ar,  $W/F_{CH_4} = 1.224 \text{ kg}_{cat} \text{ s mol}_{CH_4}^{-1}$ ) before performing partial pressure variation experiments at a total flow rate of 200 Sml min<sup>−1</sup>. The catalyst deactivation was traced by a segment under reference conditions after each partial pressure variation segment, both lasting for 30 min. The data were corrected for deactivation by the trace of methane conversion under reference conditions. All product and reactant streams were corrected by assuming the determined carbon, hydrogen, and oxygen balances, and the CO<sub>2</sub> selectivity to be equal for the raw and corrected data. Details on how these corrections were performed are found elsewhere [29].

This partial pressure variation was performed at three temperatures (i.e., 843, 858, and 873 K) in a steam-to-carbon ratio (S/C) range of 0.2–7.1, and incorporates in total 537 data points.

### 3. The microkinetic engine

The kinetic model presented in the current work has been developed using the microkinetic engine (MKE), which is an advanced (micro) kinetic modeling tool developed by Metaxas et al. [36]. The MKE can be applied for the assessment of chemical kinetics that range from simple power law models to full microkinetic models in terms of elementary steps. Implementing a kinetic model within the MKE reduces significantly the programming effort usually associated with such an application, since the tool is able to automatically translate the user supplied reaction network into a mathematical model.

More specifically, all the necessary input information, such as the number of experiments, initial parameter guesses and their respective lower and upper limits, operating conditions, experimental data, etc., are introduced in an input file. As mentioned above, the reaction network is also defined by the user, together with the list of species involved in the reaction. A distinction is made between observable species, which correspond to the experimentally measured components, and reaction intermediates, which refer to any surface species involved in an adsorption or in a surface reaction. When a catalytic reaction is modeled, the active site is always included as an additional species of the network.

When all requested input information has been successfully supplied, a FORTRAN executable is called that is responsible for the simulation of experiments and the estimation of kinetic parameters. In “simulation mode” the initial guesses of the model parameter values, as provided by the user, are applied to simulate every experiment once. For a plug flow reactor, the following set of differential equations are integrated for each bulk phase component  $i$ :

$$\frac{dF_i}{dW} = R_i \quad (1)$$

where  $F_i$  is the molar flow rate of component  $i$  ( $\text{mol s}^{-1}$ ),  $W$  is the catalyst mass (kg), and  $R_i$  is the net production rate of component  $i$  ( $\text{mol kg}^{-1} \text{s}^{-1}$ ). The net rate of formation of species  $i$  is equal to the sum of the rates of the elementary steps in which  $i$  is produced minus the rates of the elementary steps in which  $i$  is consumed:

$$R_i = \sum_j v_{ij} k_j C_{\text{obs}}^n C_{\text{int}}^m \quad (2)$$

where  $k_j$  is the rate coefficient of elementary step  $j$ ,  $v_{ij}$  the stoichiometric coefficient,  $C_{\text{obs}}$  is the concentration of the observable ( $\text{mol kg}^{-1}$ ),  $C_{\text{int}}$  is the concentration of the intermediate ( $\text{mol kg}^{-1}$ ), and  $n, m$  are the reaction orders. In case of a microkinetic reaction network, the reaction orders are all equal to stoichiometry. The pseudo-steady state approximation is made for the intermediates. Hence, their net production rate is equal to zero.

$$R_{\text{intermediate}} = 0 \quad (3)$$

The mass balance of the catalytically active sites is given by:

$$C_{\text{tot}} = C_* + \sum C_{\text{int}} \quad (4)$$

The above set of differential and algebraic equations is solved using the subroutine DASPK [37,38].

In “regression mode” the kinetic model parameters are estimated by means of two optimization subroutines. The Rosenbrock methodology [39] is used first for an initial minimization of the objective function, followed by the more sophisticated Levenberg-Marquardt method (ODRPACK 2.01 [40,41]) for the final optimization. The objective function used is the weighted residual sum of squares of the molar flow rates of the components and is minimized with respect to the unknown parameters  $b$ :

$$S(b) = \sum_{i=1}^{N_{\text{resp}}} \sum_{j=1}^{N_{\text{exp}}} w_p (F_{j,i} - \hat{F}_{j,i})^2 \rightarrow \min \quad (5)$$

where  $N_{\text{resp}}$  equals the number of responses,  $N_{\text{exp}}$  equals the number of experiments,  $\hat{F}$  represents the model calculated outlet molar flow rates and  $w_p$  are elements of the inverse of the error variance-covariance matrix, calculated from replicate experiments or estimated from the observed and calculated molar fractions at the reactor outlet, and represent the weights for each response.

After regression parity diagrams for the model responses and residual plots for the same responses as a function of the response value or of operating conditions are generated for a visual assessment of the quality of agreement between experimental observations and model calculations. Additionally, the regression is evaluated on a statistical basis using the  $F$  test for the global significance of the regression, the Student's  $t$  test for the individual significance of the model parameters and the correlation coefficient matrix for the estimated parameters [42].

### 4. Detailed reaction network and corresponding model parameters

The model established by Xu and Froment [11] served as a basis for the microkinetic model construction. Model refinements were carried out according to the experimental observations reported in [29,30] and other literature references (see second part in Section 1). A one-site model was preferred over a multi-site model, since the experimental data suggested a competition for the active site by both reactants. In the following, global (cf. Section 5.2) and elementary step (part of the network listed in Table 1) reactions are assigned by a preceding ‘R’ and ‘N’ to the reaction number, respectively, and a free surface site is represented by \* and all species having this symbol attached are adsorbed on the surface.

#### 4.1. Isotope labelling and isotopic effects

More specifically, in the investigated range of operating conditions both the steam and the methane partial pressure were found to be affecting the methane conversion. Therefore, an oxidation reaction between gas phase methane and steam derived adsorbate species was considered to be kinetically relevant [27,29,30]. Additionally, the observed isotope effects during  $\text{CH}_4/\text{CD}_4$  switch experiments at steady state throughout the whole range of S/C investigated, lead to the conclusion that a  $\text{CH}_x^*$  species has to be involved in the rate-determining step (rds), if any. Such a species was also considered to be the major intermediate for oxidation by Bradford and Vannice [43], Osaki et al. [18], and others [6,7,12,19]. The bare carbon adatom ( $\text{C}^*$ ) would not show an isotope effect during  $\text{CH}_4/\text{CD}_4$  switch experiments. Therefore, during construction of the detailed kinetic network, paths involving the oxidation of the  $\text{CH}^*$  intermediate in Reaction (N 11) were considered. In preliminary experiments, it was found, that by extrapolating the  $\text{CO}_2$  selectivity to zero conversion a value between 0.4 and 0.5 was observed. Hence, the oxidation to  $\text{CO}_2$  may not proceed solely via  $\text{CO}^*$  in a consecutive manner. A second oxidation pathway branching off from the  $\text{CHO}^*$  intermediate in Reaction (N 15) was included to produce  $\text{CO}_2^*$ , in addition to Reaction (N 17) (the  $\text{CO}^*$  oxidation). These various oxidation pathways are more clearly illustrated by different colours in the energy diagram, discussed in Section 5.3. These two oxidation reactions and the  $\text{CHO}^*$  decomposition to  $\text{CO}^*$  (Reaction (N 13)) are identical to the three kinetically relevant steps proposed in [11] by Xu and Froment.

The observed isotope effects were already discussed in the introduction. A normal isotope effect is caused by a C–H bond cleavage. Along the reaction pathway of methane steam reforming two kinds of reactions could cause such an effect: the methane dissociation (especially the initial one), and a C–H bond breaking during the reaction of a  $\text{CH}^*/\text{CHO}^*$  intermediate. Therefore, Reactions (N 3),

**Table 1**

Elementary step mechanism for methane steam reforming consisting of 12 reversible reactions, 26 of the 49 parameters, including the active site density, were fixed during the estimation process. Summary of the estimated pre-exponential factors ( $A$ ) (at average temperature  $T_{av} = 858$  K) and activation energies ( $E_a$ ) together with the 95% confidence intervals.

	Reaction	$A$ [ $s^{-1}$ ]	$E_a$ [ $kJ\ mol^{-1}$ ]
(N 1)	$CH_4 + * \rightarrow CH_4^*$	$2.87 \times 10^{3a} Pa^{-1}$	$0.0^b$
(N 2)	$CH_4^* \rightarrow CH_4 + *$	$1.0 \times 10^{13c}$	$38.5 \pm 0.16$
(N 3)	$CH_4^* + 3* \rightarrow CH^* + 3H^*$	$2.23 \cdot 10^6 \pm 4.33 \cdot 10^4\ kg\ mol^{-1}$	$87.1 \pm 2.0$
(N 4)	$CH^* + 3H^* \rightarrow CH_4^* + 3*$	$1.02 \times 10^8 \pm 4.33 \times 10^7\ g\ mol^{-1}$	$21.8 \pm 1.0$
(N 5)	$H_2O + * \rightarrow H_2O^*$	$2.7 \times 10^{3a} Pa^{-1}$	$0.0^b$
(N 6)	$H_2O^* \rightarrow H_2O + *$	$1 \times 10^{13c}$	$54.6 \pm 0.5$
(N 7)	$H_2O^* + * \rightarrow OH^* + H^*$	$1.93 \times 10^6 \pm 9.5 \times 10^4\ kg\ mol^{-1}$	$20.7 \pm 0.9$
(N 8)	$OH^* + H^* \rightarrow H_2O^* + *$	$1.04 \times 10^{10d}\ kg\ mol^{-1}$	$49.3 \pm 1.5$
(N 9)	$OH^* + * \rightarrow O^* + H^*$	$3.17 \times 10^8 \pm 9.0 \times 10^6\ kg\ mol^{-1}$	$51.3 \pm 1.0$
(N 10)	$O^* + H^* \rightarrow OH^* + *$	$1.04 \times 10^{13d}\ kg\ mol^{-1}$	$45.5 \pm 1.3$
(N 11)	$CH^* + O^* \rightarrow CHO^* + *$	$1.04 \times 10^{13d}\ kg\ mol^{-1}$	$121.0 \pm 0.8$
(N 12)	$CHO^* + * \rightarrow CH^* + O^*$	$4.03 \times 10^6 \pm 1.83 \times 10^5\ kg\ mol^{-1}$	$61.7 \pm 1.2$
(N 13)	$CHO^* + * \rightarrow CO^* + H^*$	$9.32 \times 10^5 \pm 4.33 \times 10^4\ kg\ mol^{-1}$	$104.3^e$
(N 14)	$CO^* + H^* \rightarrow CHO^* + *$	$1.04 \times 10^{13d}\ kg\ mol^{-1}$	$69.3 \pm 2.6$
(N 15)	$CHO^* + O^* \rightarrow CO_2^* + H^*$	$1.04 \times 10^{13d}\ kg\ mol^{-1}$	$83.9^e$
(N 16)	$CO_2^* + H^* \rightarrow CHO^* + O^*$	$1.04 \times 10^{13d}\ kg\ mol^{-1}$	$68.3 \pm 0.5$
(N 17)	$CO^* + O^* \rightarrow CO_2^* + *$	$1.04 \times 10^{13d}\ kg\ mol^{-1}$	$125.8^e$
(N 18)	$CO_2^* + * \rightarrow CO^* + O^*$	$1.04 \times 10^{15a}\ kg\ mol^{-1}$	$145.2 \pm 0.7$
(N 19)	$CO^* \rightarrow CO_{(g)} + *$	$1 \times 10^{13c}$	$42.3 \pm 0.07$
(N 20)	$CO_{(g)} + * \rightarrow CO^*$	$2.17 \times 10^{3a} Pa^{-1}$	$0.0^b$
(N 21)	$CO_2 \rightarrow CO_{2(g)} + *$	$1 \times 10^{13c}$	$56.9 \pm 0.8$
(N 22)	$CO_{2(g)} + * \rightarrow CO_2^*$	$1.73 \times 10^{3a} Pa^{-1}$	$0.0^b$
(N 23)	$2H^* \rightarrow H_{2(g)} + 2*$	$1.04 \times 10^{10d}\ kg\ mol^{-1}$	$45.9 \pm 1.0$
(N 24)	$H_{2(g)} + 2* \rightarrow 2H^*$	$1.87 \pm 6 \times 10^{-2}\ kg\ Pa^{-1}\ mol^{-1}$	$0.0^b$

<sup>a</sup> Fixed parameter by Eq. (9).

<sup>b</sup> Fixed parameter, non activated adsorption.

<sup>c</sup> Fixed parameter, which is the order of magnitude of  $k_b T/h$  [49].

<sup>d</sup> Fixed parameter by Eq. (10).

<sup>e</sup> Constrained by thermodynamics [50].

(N 13) and (N 15) were considered. An inverse isotope effect, which was observed at low S/C conditions, requires a reaction of a  $CH_x^*$  (possibly also a  $CH_xO^*$ ) species, which changes the hybridisation state of the carbon atom towards more p-like character, for example  $sp^2 \rightarrow sp^3$ . The only way that such a hybridisation change may occur during methane steam reforming is an oxidation reaction. Inverse isotope effects were also observed during methanation [44–47] and Fischer-Tropsch [48] reactions, however, these reactions proceed in the opposite direction of the methane steam reforming investigated in this work. Hence, Reaction (N 11) is considered in the model. The water gas shift reaction (WGS) was found not to be in equilibrium by comparing thermodynamic and experimental data [30]. Additionally,  $^{13}CO_2$  co-feed experiments were carried out and confirmed the former [29]. In agreement with Xu and Froment [11], Reactions (N 17) and (N 18) represent the WGS in the kinetic model. No H/D exchange occurred in the methane species during  $CD_4 + H_2O$  feed. The methane dissociation was therefore grouped to a single reaction step (Reaction (N 3)), since no detailed data were recorded for the several dissociation steps as by Aparicio [20], and also to avoid over-parameterization. H/D exchange, however, was observed in steam. Thus, its dissociation was considered in detail in Reaction (N 7)–(N 10). Both assumptions were supported by the results reported in [8].

#### 4.2. Model

The elementary step model consists of 12 reversible reactions including reactant and product adsorption. A scheme of the employed model is shown in Fig. 1. Two parameters per reaction, i.e., the pre-exponential factor and the activation energy, and the active site density, sum up to a total of 49 parameters. Their values for the pre-exponential factors and activation energies are listed in Table 1. 26 of those parameters were fixed and the remaining 23 parameters were estimated by regression.

The rate coefficient  $k_T$  at a temperature  $T$  is derived from Eq. (6), which is the form of the Arrhenius equation employed in

the Microkinetic engine for the reaction steps where the pre-exponential factor is estimated.

$$k_T = k_{T_{av}} \exp \left( -\frac{E_a}{R} \left( \frac{1}{T} - \frac{1}{T_{av}} \right) \right) \quad (6)$$

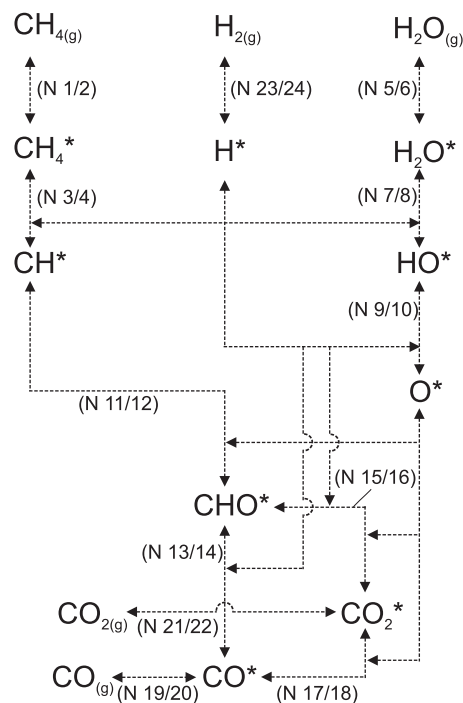


**Fig. 1.** Scheme of the employed elementary step model.  $CHO^*$  is the major intermediate along the reaction pathway.  $CO^*$  and  $CO_2^*$  are formed independently. The reaction numbers of the elementary step mechanism are indicated in parentheses (cf. Table 1).

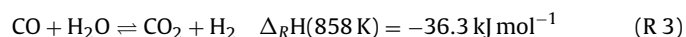
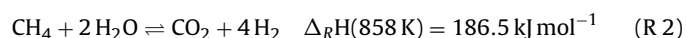
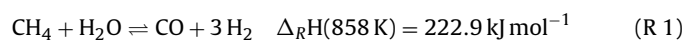


$$\frac{\partial \ln K_p}{\partial T} = \frac{\Delta_{\text{ads}} H}{RT^2} \quad (7)$$

$E_a$  is the activation energy,  $T$  the temperature in Kelvin and  $T_{\text{av}}$  and  $k_{T_{\text{av}}}$  the average temperature of investigation (i.e., 858 K), and the rate coefficient at this temperature. The adsorption enthalpies  $\Delta_{\text{ads}} H$  for the gaseous components were determined by Eq. (7) from a linear regression ( $\ln K_i$  as a function of  $1/T$ ). The adsorption coefficient  $K_i$  was calculated from the ratio of the rate coefficient in forward, and backward direction of the respective adsorption and desorption step, respectively, of species  $i$ .

The rate equations of the catalytic network were calculated, as indicated above, using Arrhenius type of equations. As mentioned above, in order to reduce the number of kinetic parameters and obtain significant estimates, various assumptions and calculations were made, that are described in the following.

Thermodynamic constraints were incorporated for the activation energies of Reactions (N 13), (N 15) and (N 17). The sum of activation energies along the pathway of Reactions (R 1), (R 2) and (R 3), were set equal to the reaction enthalpies of the overall reactions [50], i.e.,



For example: the activation energy  $E_a$  (N 13) is exclusively part of the overall reaction pathway (R 1) (not (R 2) or (R 3)); the activation energy  $E_a$  (N 13) was therefore set equal to:  $\Delta_R H(858 \text{ K})$  of Reaction (R 1) minus all other activation energies along this reaction pathway (cf. Fig. 1), that is:

$$\begin{aligned} E_a(\text{N}13) = & 223.084 - E_a(\text{N}1) + E_a(\text{N}2) - E_a(\text{N}3) + E_a(\text{N}4) \\ & - E_a(\text{N}11) + E_a(\text{N}12) - E_a(\text{N}5) + E_a(\text{N}6) - E_a(\text{N}7) \\ & + E_a(\text{N}8) - E_a(\text{N}9) + E_a(\text{N}10) + E_a(\text{N}14) - E_a(\text{N}20) \\ & + E_a(\text{N}19) - 3 * E_a(\text{N}24) + 3 * E_a(\text{N}23) \end{aligned} \quad (8)$$

Similar constraints were derived for  $E_a$  (N 15) and  $E_a$  (N 17) based on reaction pathways (R 2) and (R 3), respectively.

Molecular adsorption was assumed for  $\text{H}_2\text{O}$ ,  $\text{CO}$ ,  $\text{CO}_2$  [11,20,23], and  $\text{CH}_4$  [11,23,51], whereas  $\text{H}_2$  was assumed to dissociate upon adsorption [20,23]. All of the adsorption steps of the gas species ( $\text{CH}_4$ ,  $\text{H}_2\text{O}$ ,  $\text{CO}$ ,  $\text{CO}_2$ , and  $\text{H}_2$ ) were assumed to be non-activated ones, hence their activation energies were set equal to zero. Additionally, collision theory was used to calculate the maximum value of the pre-exponential factors. In this work, these pre-exponential factors were assumed to be equal to the collision frequency and were calculated according to the following equation [49]:

$$k_i = \frac{S_p}{\sigma} \frac{1}{\sqrt{2\pi MRT}} \quad (9)$$

where  $k_i$  is the pre-exponential factor of adsorption reaction  $i$  [ $\text{Pa}^{-1} \text{s}^{-1}$ ];  $R$  is the universal gas constant [ $\text{J mol}^{-1} \text{K}^{-1}$ ];  $T$  is the temperature and assumed equal to the average of the experimental range investigated, i.e., 858 K;  $M$  is the molar mass of the gas species [ $\text{kg mol}^{-1}$ ];  $S_p$  is the catalyst specific surface area determined via the BET method,  $740 \text{ m}^2 \text{ kg}_{\text{cat}}^{-1}$  [30];  $\sigma$  is the active site density determined from  $\text{O}_2$  chemisorption measurements,  $9.654 \times 10^{-3} \text{ mol-surf-Ni kg}_{\text{cat}}^{-1}$  [29].

The pre-exponential factors for molecular desorption reactions were calculated according to transition state theory, assuming a similar degree of mobility between the adsorbed species and the transition state. Hence, they were set equal to  $10^{13} \text{ s}^{-1}$ , which is the order of magnitude of  $k_b T/h$  [49],  $k_b$  being the Boltzmann constant [ $\text{J K}^{-1}$ ];  $h$  the Plank constant [ $\text{J s}$ ]. Finally, for the pre-exponential

factors of reactions involving two surface species it was assumed that the involved species are mobile on the surface, while, similarly, for the associative desorption of  $\text{H}_2$  completely mobile surface species and transition states were considered. Hence, the following equation was applied [49]:

$$k_i = \frac{N_A k_b T}{S_p h} \frac{Q_{AB^\ddagger}}{Q_{A^*} Q_{B^*}} \quad (10)$$

where  $k_i$  is the pre-exponential factor of reaction  $i$  [ $\text{kg mol}^{-1} \text{s}^{-1}$ ];  $N_A$  the Avogadro constant [ $\text{mol}^{-1}$ ],  $Q_i^\ddagger$  the molecular partition functions of the involved species per unit area [ $\text{m}^{-2}$ ] ( $AB^\ddagger$  being the activated complex and  $A^*$ ,  $B^*$  the surface species taking part in the reaction).

Generally, reactions with high activation barriers are considered to be significant for the overall kinetics. This criterion does, however, not give the full information needed and might mislead the interpretation. A combination of the net rate, and approach to partial equilibrium (PE), in contrast, comprises the essential information required. Hence, for an elementary step to be kinetically significant, firstly it needs to be far away from partial equilibrium, and, secondly, proceed with a low net rate (with respect to the remaining reactions in the investigated network).

## 5. Model simulation results

### 5.1. Comparison to experimental data

Table 1 shows the finally estimated values for the pre-exponential factors and the activation energies. The 95% confidence intervals are sufficiently narrow, ensuring low standard errors. The maximum absolute value in the correlation coefficient matrix amounts to 0.78 and occurs between the pre-exponential factor, A (N 4), and the activation energy  $E_a$  (N 13). Hence, it can be concluded that no significant correlation between the model parameters occurs. The model's good performance is confirmed by the squared multiple correlation coefficient being close to unity ( $R^2 = 0.998$ ), and a high  $F$  value ( $2.96 \times 10^4$ ) for the global significance of the regression (tabulated value = 2.79).

In Fig. 2 the parity diagrams are illustrated for all gaseous components. All simulated outlet concentrations were qualitatively correct. The dataset's different temperatures were equally well described by the model. The highest deviations were observed for CO (cf. Fig. 2(d)), which is the component with the highest experimental uncertainty. The  $\text{CO}_2$  selectivities for 873 K and 858 K were qualitatively and quantitatively well predicted by the model shown in Fig. 3(a) and (b). At 843 K a deviation at high S/C ratios was observed (cf. Fig. 3(c)), in which the model predicted higher  $S(\text{CO}_2)$  values compared to the experimental data.

In the following, the focus will be on the comparison between experimental and model simulated turnover frequencies. The data was subdivided into three kinetic regimes, as described in [29] (Figs. S2 and S3 in this reference), in low, intermediate, and high S/C range. A summary of S/C ranges, kinetic orders, and kinetic coefficients for all three investigated temperatures is collected in Table 2. The deviation (absolute values) of simulated to experimentally determined TOFs were in average (summarising all 537 data points)  $0.32 \text{ s}^{-1}$  and  $0.52 \text{ s}^{-1}$  with a maximum of  $1.24 \text{ s}^{-1}$  and  $2.08 \text{ s}^{-1}$  for  $\text{TOF}(\text{CH}_4)$  and  $\text{TOF}(\text{H}_2\text{O})$ , respectively, which underlines the quality of the applied model. Highest deviations were observed at low S/C ratios for  $\text{TOF}(\text{H}_2\text{O})$  and high S/C ratios for  $\text{TOF}(\text{CH}_4)$ . This can be explained by the increasing experimental error of determining low reactant partial pressures, i.e. low and high S/C. The kinetic orders of both reactants were observed independent of temperature at low S/C ratios (i.e. first regime), cf. Table 2. In the second and third regime (i.e. intermediate and high S/C ratios) the kinetic order

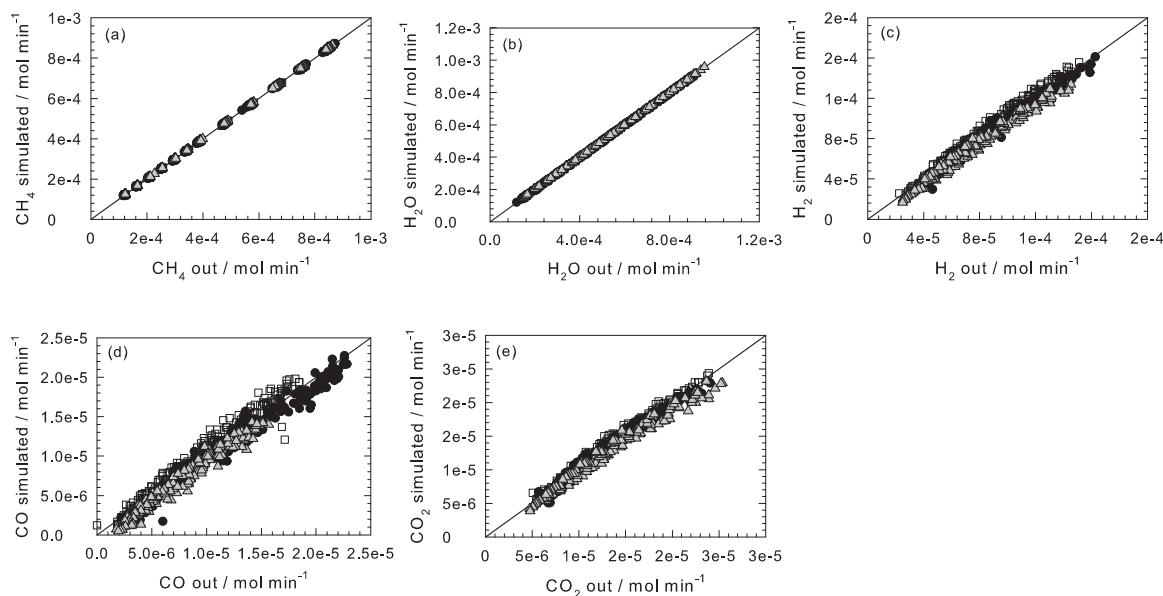


**Fig. 2.** Parity diagrams of all gaseous components. The line represents the so-called “parity” and should be approached by the symbols which are representing the model simulations. The colour of the symbols represents the temperature of investigation (black circle) 873 K, (white square) 858 K, and (gray triangle) 843 K.

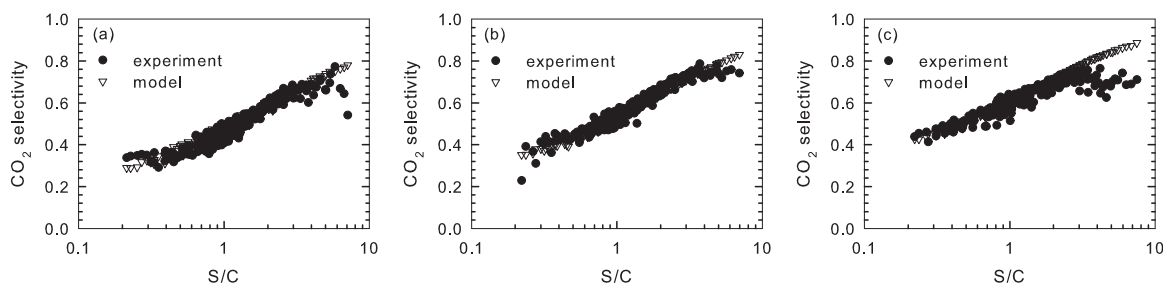


**Fig. 3.**  $\text{CO}_2$  selectivity as a function of the steam to carbon inlet ratio: Comparison between experiment (black circle) and model (white triangle) data for (a) 873 K, (b) 858 K, and (c) 843 K.

of methane increases, whereas that of steam decreases simultaneously ( $0.4 \rightarrow 0.7$ ,  $0.6 \rightarrow 0.8$ , and  $0.2 \rightarrow -0.1$ ,  $-0.1 \rightarrow -0.3$ , respectively) with decreasing temperature. The supplementary information contains the remaining illustrations for methane and steam turnover frequencies at 858 K and 843 K in Figs. S1 and S2, respectively.

## 5.2. Surface coverage

All surface intermediates coverages are shown in Fig. 5 as a function of S/C. The intermediates with a coverage exceeding  $5 \times 10^{-4}$  are illustrated in Fig. 5(a). The total surface coverage does not

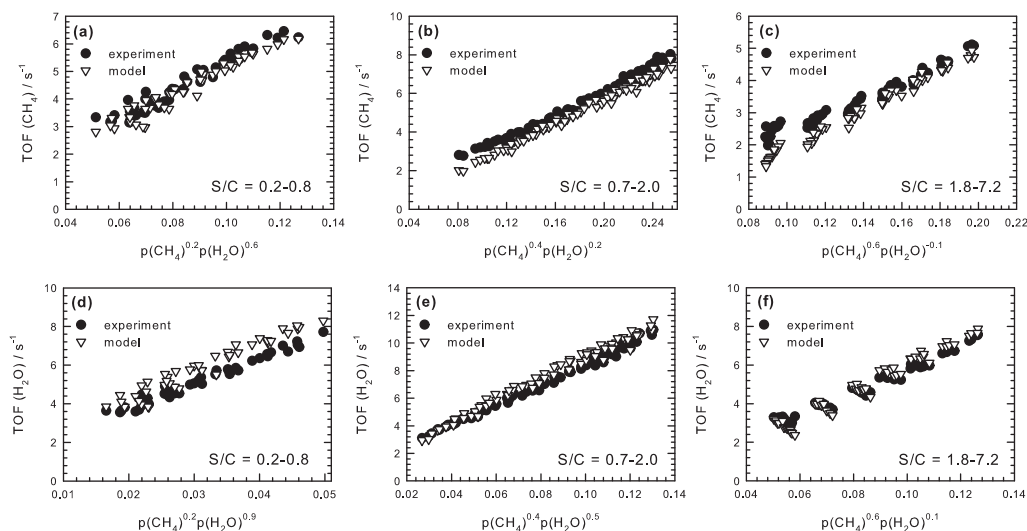


**Fig. 4.** Experimental and simulated turnover frequencies 873 K, subdivided into three kinetic regimes (i.e. S/C ranges of 0.2–0.8 (a and d), 0.7–2 (b and e), and 1.8–7.2 (c and f), as described in [29]) for methane (a–c) and steam (d–f), respectively. Kinetic orders of the reactants are averaged values determined in each of the kinetic regimes. Kinetic constants and kinetic orders are summarised and compared in Table 2.

**Table 2**

Methane and steam partial reaction orders and corresponding global kinetics coefficient as directly determined from the experimental data in Figs. 4, S1 and S2 as well as by regression of the power-law equation  $\text{TOF} = k p(\text{CH}_4)^n p(\text{H}_2\text{O})^m$  to the corresponding mke simulations (See Section 5.1).

Temperature	S/C range	TOF	$n$	$m$	Data	$k/\text{s}^{-1} \text{bar}^{-(n+m)}$	$r^2$
873 K	0.2–0.8	$\text{CH}_4$	0.2	0.6	exp	53.6	0.941
					mke	51.4	0.940
		$\text{H}_2\text{O}$	0.2	0.9	exp	161.3	0.887
					mke	180.7	0.862
	0.7–2	$\text{CH}_4$	0.4	0.2	exp	30.4	0.982
					mke	28.4	0.979
		$\text{H}_2\text{O}$	0.4	0.5	exp	85.4	0.963
					mke	90.5	0.957
	1.8–7.2	$\text{CH}_4$	0.6	−0.1	exp	24.6	0.960
					mke	22.3	0.908
		$\text{H}_2\text{O}$	0.7	0.1	exp	57.3	0.971
					mke	58.9	0.936
858 K	0.2–0.8	$\text{CH}_4$	0.2	0.6	exp	42.9	0.943
					mke	45.4	0.956
		$\text{H}_2\text{O}$	0.2	0.9	exp	132.5	0.862
					mke	163.2	0.854
	0.7–2	$\text{CH}_4$	0.5	0.1	exp	24.8	0.980
					mke	25.5	0.975
		$\text{H}_2\text{O}$	0.5	0.4	exp	74.1	0.946
					mke	82.9	0.973
	1.8–7.2	$\text{CH}_4$	0.8	−0.2	exp	28.9	0.972
					mke	29.2	0.968
		$\text{H}_2\text{O}$	0.8	0.0	exp	70.7	0.962
					mke	79.1	0.983
843 K	0.2–0.8	$\text{CH}_4$	0.2	0.6	exp	45.2	0.940
					mke	41.7	0.979
		$\text{H}_2\text{O}$	0.2	0.9	exp	147.1	0.923
					mke	159.8	0.850
	0.7–2	$\text{CH}_4$	0.7	−0.1	exp	25.8	0.859
					mke	23.4	0.960
		$\text{H}_2\text{O}$	0.7	0.1	exp	62.6	0.958
					mke	62.9	0.961
	1.8–7.2	$\text{CH}_4$	0.8	−0.3	exp	21.5	0.959
					mke	19.3	0.938
		$\text{H}_2\text{O}$	0.8	−0.1	exp	52.1	0.980
					mke	54.4	0.959

exceed 0.4 and, hence, the fraction of free surface sites (\*) is always  $\geq 0.6$ .  $\text{CH}^*$  and  $\text{O}^*$  were the most abundant surface species with a maximum coverage of 0.4 and 0.2, respectively. The evolution in their surface concentrations intersects at S/Cs of 1.5–2. At low S/Cs the only significant species was  $\text{CH}^*$ , whereas at high S/Cs both  $\text{O}^*$  and  $\text{OH}^*$  show an almost identical abundance. That of the hydrogen atoms ( $\text{H}^*$ ) was independent of the S/C and shows a minor response to the total reactant partial pressure. All other surface species concentrations change significantly, affected by the applied reaction conditions. Surface coverages lower than  $5 \times 10^{-4}$  are presented in Fig. 5(b). Both carbon oxides ( $\text{CO}^*$  and  $\text{CO}_2^*$ ) have negligible

coverages. Adsorbed steam has an abundance of about one order of magnitude higher compared to adsorbed methane.  $\text{CO}_2^*$  has a low coverage, partly lower than the reactants.

### 5.3. Kinetic relevance of the surface reactions

The reaction network introduced in Fig. 1 consists of 24 elementary reaction steps. The three elementary reactions showing the highest activation barriers were Reactions (N 11), (N 17) and (N 18). The energy diagram in Fig. 6 depicts the activation energies of Table 1. The black colour indicates the pathway to the  $\text{CHO}^*$

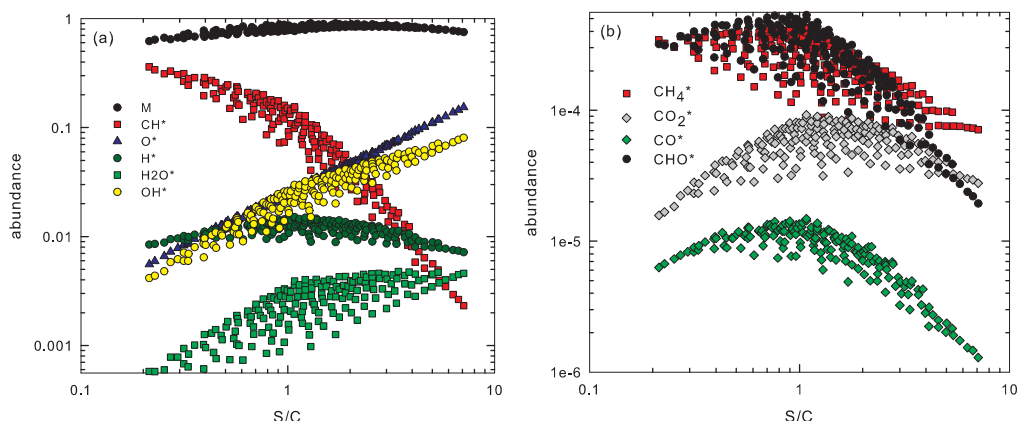


**Fig. 5.** Surface intermediates coverages at 873 K: (a) higher coverage,  $\geq 5 \times 10^{-4}$ , where M represents free surface sites; (b) lower coverage,  $\leq 5 \times 10^{-4}$ .

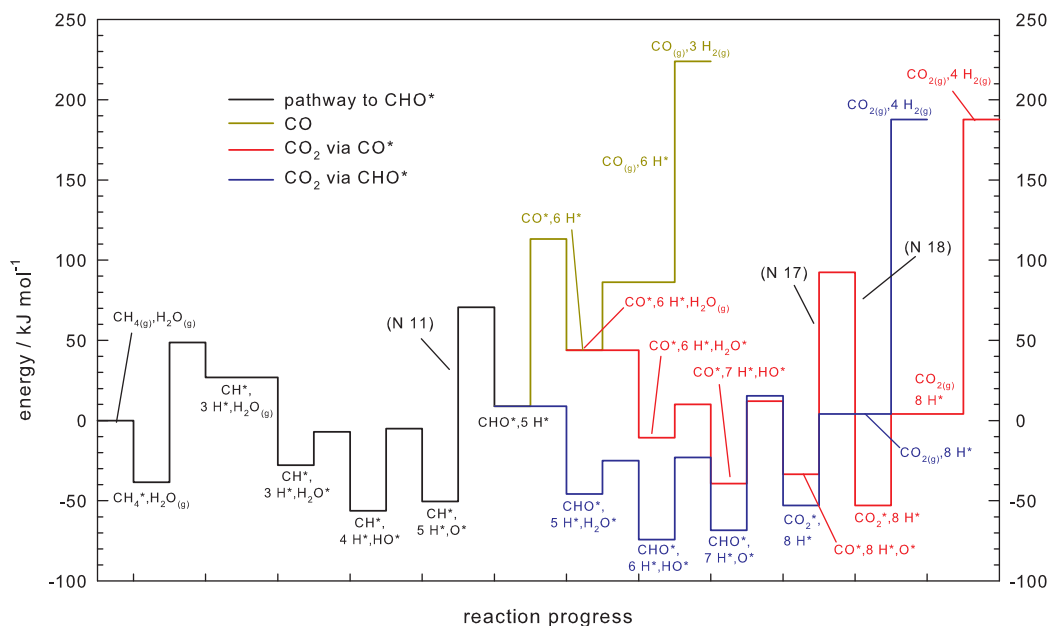


**Fig. 6.** Energy diagram of the investigated reaction network according to the values summarised in Table 1: (black) pathway to  $\text{CHO}^*$ ; (dark yellow) CO formation; (red)  $\text{CO}_2$  formation via  $\text{CO}^*$ ; (blue)  $\text{CO}_2$  formation via  $\text{CHO}^*$ . (For interpretation of the references to color in this text, the reader is referred to the web version of the article.)

intermediate, which branches into the  $\text{CO}^*$  formation (dark yellow) and one  $\text{CO}_2^*$  formation pathway (blue). From the  $\text{CO}^*$  species another branch to  $\text{CO}_2^*$  departs (red). Due to the constraint explained above the energy difference between initial and final states is consistent with thermodynamics.

Each surface reaction appears with a forward and backward rate ( $r_f$  and  $r_b$ , respectively). Two parameters to categorise the surface reactions are: the partial equilibrium ratio and the net rate. The former describes the direction, showing whether the reaction proceeds in forward or reverse direction, or is in partial equilibrium. The partial equilibrium (PE) ratio,  $\phi$ , is, therefore, defined by the ratio of the forward to the sum of forward and backward rate ( $r_f/(r_f + r_b)$ ) [52]. The net rate shows how fast the reaction proceeds ( $|r_f - r_b|$ ). In Fig. 7 the net rate is plotted as a function of the S/C for 873 K. Figs. S4 and S5, in the supplementary information, show the variations of the PE ratio and net rate as a function of S/C ratio at different temperatures, respectively.

Fig. 7(a) depicts the dissociation of the reactants. Both reactions have the same net rate at low S/C and differ with about 2 orders of magnitude at high S/C. The oxidation reactions (with  $\text{O}^*$ ) of  $\text{CH}^*$  and  $\text{CHO}^*$  were fastest in Fig. 7(b), whereas the  $\text{CHO}^*$  dissociation was slower and  $\text{CO}^*$  oxidation was slowest. The temperature dependence of these reactions is presented in Fig. S5, which is practically negligible.

The colour coding of the symbols represents the direction of the elementary step (purple – backward and, across the rainbow, red – forward). Fig. S3 illustrates solely the PE as a function of S/C. It might, therefore, be employed together with Fig. 7 for a clearer interpretation of the complex relations. In Fig. 7(a), the steam dissociation is closest to partial equilibrium, independently of the S/C. Methane dissociation behaves differently. It is closest to equilibrium at low S/C, whereas it reacts exclusively forward at high S/C.

The situation is more complex for the oxidation reactions, illustrated in Fig. 7(b). The  $\text{CH}^*$  oxidation (Reactions (N 11) and (N 12)) is close to partial equilibrium and at low S/Cs proceeding with a net rate that is one order of magnitude higher compared to the  $\text{CHO}^*$  oxidation (Reactions (N 15) and (N 16)). The latter is also close to partial equilibrium for all reaction conditions and having the same net rate as the  $\text{CH}^*$  oxidation at high S/C. The  $\text{CO}^*$  and  $\text{CO}_2^*$  formation from  $\text{CHO}^*$  (Reactions (N 13) and (N 14) and Reactions

(N 15) and (N 16), respectively) are competing at low S/Cs, where the former is proceeding in forward direction and the latter is close to partial equilibrium. The  $\text{CO}^*$  oxidation (Reactions (N 17) and (N 18)) proceeds exclusively backwards, thus,  $\text{CO}^*$  is formed from  $\text{CO}_2^*$  dissociation. Due to its low net rate, however, this reaction does not contribute significantly to the overall reaction.

The adsorption coefficients were determined according to Eq. (6), and the adsorption enthalpies by the van't Hoff equation (cf. Eq. (7)). All adsorption enthalpies observed were (as expected) negative:  $-38.5$  ( $\text{CH}_4$ ),  $-54.6$  ( $\text{H}_2\text{O}$ ),  $-45.9$  ( $\text{H}_2$ ),  $-42.0$  ( $\text{CO}$ ), and  $-56.9$  ( $\text{CO}_2$ )  $\text{kJ mol}^{-1}$  in the temperature range 843–873 K (cf. Table 3).

## 6. Discussion

The applied elementary step model with the estimated pre-exponential factors and activation energies describes the experimental data quite satisfactorily. Methane and steam turnover frequencies (cf. Fig. 4) follow the experimental values qualitatively and quantitatively, with an average (absolute value) and maximum deviation of  $0.32 \text{ s}^{-1}$  and  $0.52 \text{ s}^{-1}$  with a maximum of  $1.24 \text{ s}^{-1}$  and  $2.08 \text{ s}^{-1}$  for  $\text{TOF}(\text{CH}_4)$  and  $\text{TOF}(\text{H}_2\text{O})$ , respectively. The methane TOF is described very well for low and intermediate S/Cs. At high S/Cs the simulated TOF is slightly below the experimental observations. However, the trend and quantity of steam TOF and  $\text{CO}_2$  selectivity is modeled correctly. Thus, the lower methane conversion does not affect the  $\text{CO}_2$  selectivity. It solely provides less carbon intermediates for oxidation than required to reach the experimental conversion. Hence, the amount of carbon intermediates on the surface is not determining for adequately simulating the subsequent oxidation reactions. Thus, the availability of surface oxygen determines the rate of surface oxidation reactions, which was also concluded by Aparicio [20] and Maier et al. [23]. More generally, it was concluded, that the availability of this surface oxygen depends on the nature of the support, which plays a key role for the water adsorption/dissociation [20]. Water is expected to compete with methane for the active site on the nickel surface, in case rather inert support materials are employed like spinel-type materials [11,29,51] or unsupported nickel [4,5]. Other support materials may facilitate the water adsorption, hence, the water partial pressure becomes kinetically irrelevant in the overall rate expression



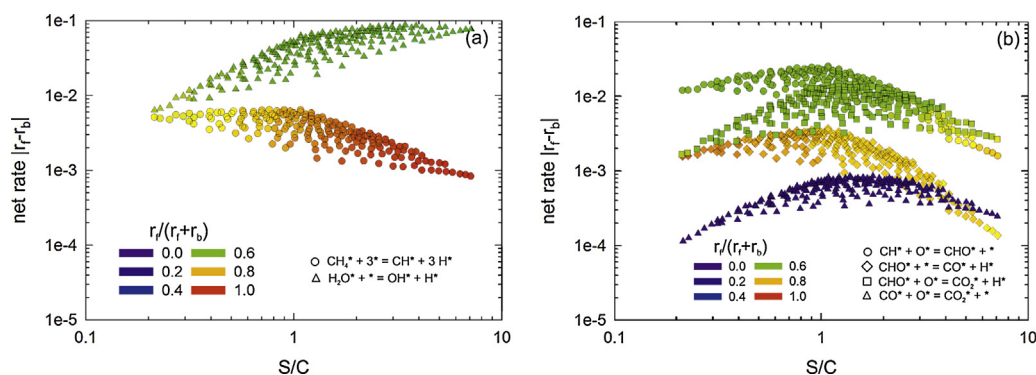


**Fig. 7.** Net rate of surface reactions at 873 K as a function of S/C. The colour of the symbols indicates the direction (forward or backward), the sole direction of the surface reactions is shown in the supplementary information in Fig. S3. (For interpretation of the references to color in this text, the reader is referred to the web version of the article.)

[9,13]. The results of the model presented here are expected to differ in case of facilitated water adsorption by the support material [20]. All reactions involving an adsorbed oxygen atom would be expected to increase in rate, and additionally show much less dependency on the applied S/C ratio (cf. Fig. 7).

Parity diagrams in Fig. 2 show a good qualitative if not quantitative match between experiment and model simulations. The presented fit is a compromise of variously weighted product and reactant partial pressure considerations applied during the estimation procedure. From an experimental point of view the CO partial pressure is, as mentioned, the least trustworthy of all components.

The surface coverage was calculated  $\leq 20\%$  for  $S/C \geq 0.6$  (cf. Fig. 5), and is in agreement with literature [24,27], which commonly reports low coverages during methane steam reforming conditions, especially at  $T \geq 600^\circ\text{C}$ . In agreement with Maestri et al. [52], we expect for the presented experimental conditions [29] a negligible influence of surface coverage on the estimated kinetic parameters for the overall reaction. The kinetic parameters determined by Aparicio et al. were also independent of any surface coverage values [20]. The surface coverage of CO was part of the microkinetic model of Maier et al. [23], however, the most sensitive elementary reaction steps on the methane mole fraction were found to

be independent of the CO coverage. Nonetheless, it should also be mentioned that even though such low coverages were observed, a simultaneous competition for adsorption centres by both reactants could be determined [11,29,51].

Our results show at high S/C ratios  $\text{O}^*$ ,  $\text{OH}^*$ , and  $\text{H}^*$  to be the most abundant surface species (cf. Fig. 5). Maier et al. [23] found  $\text{H}^*$ ,  $\text{CO}^*$ , and  $\text{O}^*$  as most abundant surface species as a result of their microkinetic approach, which was similar to the DFT calculations on Ni(111) by Blaylock et al. [24], who found  $\text{H}^*$ ,  $\text{CO}^*$ , and  $\text{H}_2\text{O}^*$  most abundant. In both references, a larger activation energy for  $\text{H}_2\text{O}^*$  dissociation was employed, which were  $91.76 \text{ kJ mol}^{-1}$  [23] and  $89 \text{ kJ mol}^{-1}$  [24], respectively, compared to  $20.7 \text{ kJ mol}^{-1}$  listed for our model in Table 1. Furthermore, their reported results were obtained at higher temperatures ( $1120 \text{ K}$  [23] and  $1073 \text{ K}$  [24]) and especially higher methane conversion levels of  $>70\%$ , for which an increased partial pressure of  $\text{H}_2$  and  $\text{CO}$  in the reactive atmosphere could be expected. Thus, it may explain the different findings in comparison to our reported work ( $873 \text{ K}$  and methane conversions  $\leq 12\%$ ). A negligible  $\text{O}^*$  coverage was reported by Avestisov et al. [13], surprisingly for a S/C of 4, which is in contrast to Xu and Froment [11] and our findings. Chen et al. [26] reported an abundance of  $\text{C}^*$  (which was simulated of experimental data from Xu

**Table 3**

Adsorption enthalpies given in  $[\text{kJ mol}^{-1}]$ : the first two parts are experimental model data, the third part summarizes values determined by calorimetry and other experimental methods. The last part incorporates values from microkinetic models.

$\Delta_{\text{ads}}H_{\text{CH}_4}$	$\Delta_{\text{ads}}H_{\text{H}_2\text{O}}$	$\Delta_{\text{ads}}H_{\text{H}_2}$	$\Delta_{\text{ads}}H_{\text{CO}}$	$\Delta_{\text{ads}}H_{\text{CO}_2}$	Temperature [K]	Refs.
-38.5	-54.6	-45.9	-42.3	-56.9	843–873	This work
-38.28	88.68	-82.9	-70.65		648/823	[11]
	15.9	-93.4	-140		673/823	[12]
	54.4		-19.6		648	[51]
			-100 – -140		Room temp.	[53]
			-120		308	[54]
			-123 – 133		300	[55]
			-122			[56]
			-96.3			[57]
		-65.3 – -83.74				[58,59]
	-38.4 / -61.98				298 / 573	[60]
	-87.73 <sup>a</sup>				873 <sup>b</sup>	[60]
		-93.3				[57]
		-41.87	-146.54			[61]
	-50 – -59	-100.5				[62]
	-92 – -100					[62]
		-96.7			287 – 473	[63]
-25.12	-71.18		-113.04			[64]
	64.4	95	115			[20]
	38/91					[25]
37.55	60.79	81.21	111.27 <sup>b</sup>	25.98	900 – 1200	[23]

<sup>a</sup> Extrapolated.

<sup>b</sup> Coverage dependent.

and Froment [11]) of 0.01–0.02 at  $S/C=3$  and comparable space velocity (i.e., 0–0.4 g h mol<sup>-1</sup> and in our case 0.34 g h mol<sup>-1</sup>, however at 15 bar, compared to 1 bar in our experiments). This agreed well with the value of 0.01–0.02 observed in Fig. 5 for CH\* (which was the most carbon-like species in our model). Due to the co-feed of hydrogen during the experiments [11], a much higher simulated H\* coverage was reported in comparison to our values (which were obtained without hydrogen co-feed). The significance of such hydrogen co-feed on the kinetics of methane steam reforming was discussed by Sprung et al. [29].

Activation energies of key reactions, such as Reactions (N 2), (N 6) and (N 17) were estimated in good agreement (i.e. 38.5/37.6, 54.6/60.8, and 125.8/123.6 kJ mol<sup>-1</sup>, respectively) to those reported by Maier et al. [23]. For another reaction, the formation of CHO\* from CO\* and H\*, a rather different value of 69.3 kJ mol<sup>-1</sup> was estimated in this work, which was about half the value of their model (i.e. 132.2 kJ mol<sup>-1</sup>) and more than twice in comparison to the predictions by Aparicio et al. (i.e. 23 kJ mol<sup>-1</sup>) [20]. All three models, however, are based on different reaction networks and formation reactions to key intermediates. Therefore, a variation of parameter estimates can be expected. Both Maier et al. [23] and Aparicio et al. [20] consider first the oxidation of a C\* species, rather than a CH<sub>x</sub>\* species, as presented in Fig. 1. The activation energy of the first oxidation step of the current work (Reaction (N 11)) was 121 kJ mol<sup>-1</sup> and, hence, closer to the one found by Maier et al. (148 kJ mol<sup>-1</sup>) [23] (in Aparicio et al. a value of 65 kJ mol<sup>-1</sup> is reported [20]). Additionally, in both of these cited works the experiments were carried out at higher temperatures and, hence, at conditions much closer to thermodynamic equilibrium compared to the work presented here.

A summary of the adsorption enthalpies found in this study is given in Table 3 in comparison to other results reported in the literature. Xu and Froment [11] used an elementary step model close to the one in this study. The methane adsorption enthalpy as determined by Xu and Froment is in good agreement with our results. Their values for H<sub>2</sub> and CO adsorption are, however, significantly higher. Compared to calorimetric studies, our adsorption enthalpy for methane is a good approximation and so is the one for H<sub>2</sub>O. Our adsorption enthalpies for the products H<sub>2</sub> and CO were within the range of reported values (cf. Table 3). The deviations may be explained by the way the activation energies are determined in the model in Table 1. The activation energies were assumed to be independent of the surface coverage, hence, this could alter the adsorption enthalpy [23].

Energy diagrams, as the one in Fig. 6, represent a static view on the reaction network. Data sets incorporating a wide range of reaction conditions may not be interpreted properly, since dynamic (i.e. changing reaction conditions) information is invisible. Our methodology, illustrated in Fig. 7, combines two parameters; the net rate and the approach to partial equilibrium (PE), which comprises the essential information required. In the experimental work, a normal isotope effect was observed at high  $S/C$  [29], thus, a kinetically relevant reaction with a C–H bond cleavage is needed. Fig. 7 shows three reactions fulfilling the criteria mentioned above. These are the CH<sub>4</sub>\* dissociation, the CHO\* dissociation to CO, and the CHO\* oxidation to CO<sub>2</sub>. All are part of the major reaction pathway. The two former reactions proceed forward, whereas the latter is close to partial equilibrium. Additionally, the CH<sub>4</sub>\* and CHO\* dissociation have a similarly low net rate and can, hence, be held responsible for the observed normal isotope effect at high  $S/C$  ratios, while the CHO\* oxidation step does not contribute to this effect. This is in accordance with the general conclusion of several elementary steps being kinetically significant [20,22,27,43]. These elementary steps are preferably the methane dissociation and an oxidation reaction. The nature of the latter depends on the considered intermediate species in the developed models. C\* [20,22,27] and CH\* [24,43] are

potential intermediates when the first oxidation step is considered kinetically significant. Several reaction networks, also our network (cf. Fig. 1), include the second oxidation step as kinetically relevant [11,12]. Thus, this supports the assumption that also the direct oxidation route contributes significantly to form CO<sub>2</sub> from methane [11,12,16,65].

At low  $S/C$ s the CH<sub>4</sub>\* dissociation is closer to partial equilibrium than at high  $S/C$ s. The situation is different for the CHO\* dissociation to CO\*. The CHO\* formation and CHO\* oxidation to CO<sub>2</sub>\* are still close to partial equilibrium and are for now not considered in the discussion for kinetically relevant steps. The CO\* formation from CHO\* is, therefore, most likely to be kinetically relevant, also since it is part of the major reaction pathway. However, at low  $S/C$  an inverse kinetic isotope effect (KIE) needs to be explained. Both suggested kinetically relevant steps do involve a C–H bond cleavage, which causes a normal KIE.

An inverse kinetic isotope effect requires a C–H centre where a reaction takes place, without cleaving the C–H bond. Reaction (N 11) would be suitable to be at the origin of an inverse KIE, however, this reaction is in partial equilibrium. Somehow, this observed isotope effect needs to be reflected in the simulation results. A possibility would be to approach this issue from a different angle and consider a thermodynamic (or equilibrium) isotope effect. Some of the surface reactions are found to be in or very close to partial equilibrium. Thus, considering a thermodynamic isotope effect in addition may be reasonable. It can be suspected, that this equilibrium (Reaction (N 11) and (N 12)) is slightly more shifted to the product side when protium is substituted by deuterium. In comparison to the remaining oxidation reactions in Fig. 7(a), this reaction has a two orders of magnitude higher net rate. An increase of the coverage of the CHO\* (CDO\*) intermediate would, therefore, accelerate the successive decomposition and oxidation reactions. Thus, the methane conversion increases when CH<sub>4</sub> is replaced by CD<sub>4</sub> in the steam reforming reaction at low  $S/C$ .

Even if the explanation of the inverse isotope effect caused by an equilibrium shift sounds reasonable, the reforming of methane still requires C–H bond cleavage steps in the reaction pathway, explained above. This discrepancy needs to be unified. A tentative interpretation is made based on the concept pioneered by Kiperman [34]. There, the observed isotope effect is a product of the kinetic and thermodynamic isotope effect. Based on the pure numbers, which are an observed inverse isotope effect (0.9 [29]), and determined/expected for the normal isotope effect (1.3 [29] and references therein), the expected TIE would have a value of 0.69 (exponent  $n=1$ , see [34]). This value is assumed to be acceptable, however, not proven. Until other explanations describe the observations at low  $S/C$  reported in [29] in combination with this work in a different way, our interpretations are considered reasonable.

On the base of Fig. 7, CHO\* is the main intermediate, in agreement with Bradford and Vannice [43], which may decompose to CO\* or be oxidised to CO<sub>2</sub>. At low  $S/C$ s both pathways proceed, however, the dissociation to CO\* is irreversible. For high  $S/C$ s the CHO\* oxidation is preferred over the decomposition by an order of magnitude higher net rate, supporting the observations made by Akers and Camp [65]. Thus the CHO\* oxidation is considered the main pathway. In other models, a carboxylate species (COOH\*) was considered to be the main oxygen containing intermediate [20,21,24,26,28]. Such a common oxygen containing intermediate (preferably other than CO<sub>2</sub>\* since that is in equilibrium with the gas phase) is required, to form CO\* and CO<sub>2</sub>\* independently [66].

The obtained results for this 2 wt% NiO/NiAl<sub>2</sub>O<sub>4</sub> steam reforming catalyst are expected to be valid for higher loadings of nickel on the same (hence, an inert) support material. Nickel particles were

found to be in close contact with each other on the employed 2 wt% catalyst (cf. Section 7.4 on SEM characterisation in [35]). An increase in nickel loading, thus, might not change this particular interaction. Hence, the determined kinetic dependencies of both reactants are expected to remain similar.

## 7. Conclusions

A thermodynamically consistent microkinetic model for methane steam reforming was presented, based on an extensive experimental data set. The simulated turnover frequencies for methane and steam and CO<sub>2</sub> selectivities were qualitatively if not quantitatively in very good agreement with the experimental data. All partial pressures were described correctly.

The central question of our investigation was to explain by microkinetic modelling the observed change in kinetic regimes, depending on the applied reaction conditions. A dynamic view was established, which combines the net rate and direction (i.e. approach to partial equilibrium) of a specific reaction step in one diagram. Thus, it was possible to follow how these two parameters changed with the applied reaction conditions.

The disappearance of the experimentally observed normal kinetic isotope effect with decreasing S/C ratio could be attributed to the following two reaction steps: For the CH<sub>4</sub>\* dissociation reaction the net rate decreased and its direction changed from forward towards partial equilibrium. Furthermore, the CHO\* oxidation reaction (a core intermediate in our reaction scheme) appeared with a high net rate. The combined view on the approach to partial equilibrium and the net rate highlighted the significance of the second oxidation step (CHO\* + O\*) compared to the commonly considered step (C\*/CH\* + O\*).

A qualitative explanation was proposed for the origin of the experimentally observed inverse kinetic isotope effect at low S/C. The reaction steps, which could potentially cause such an effect (i.e. CH\* oxidation to CHO\*), were found to be in partial equilibrium under all experimental conditions. It is, therefore, proposed, that a thermodynamic (i.e. equilibrium) isotope effect could be the reason for the experimental observation. Hence, it could disguise the underlying normal isotope effect, caused by C–H bond cleavage reaction steps, due to its high net rate.

## Acknowledgements

The Norwegian Research Council, through the RENERGI project “Hydrogen Production by Sorbent Enhanced Reforming”, P 178129/S30, is acknowledged for financial support.

This paper reports work undertaken in the context of the project OCMOL, Oxidative Coupling of Methane followed by Oligomerization to Liquids. OCMOL is a Large Scale Collaborative Project supported by the European Commission in the 7th Framework Programme (GA no. 228953). For further information about OCMOL see: <http://www.ocmol.eu> or <http://www.ocmol.com>.

## Appendix A. Supplementary data

Supplementary data associated with this article can be found, in the online version, at <http://dx.doi.org/10.1016/j.apcata.2014.10.062>.

## References

- [1] Key World Energy Statistics, International Energy Agency, 2013 <http://www.iea.org/publications/freepublications/publication/KeyWorld2013.pdf>
- [2] J.R. Rostrup-Nielsen, J. Sehested, J.K. Nørskov, *Adv. Catal.* 47 (2002) 65–139.
- [3] J. Rostrup-Nielsen, L.J. Christiansen, *Catalytic Science Series: Concepts of Syngas Manufacture*, vol. 10, Imperial College Press, 2011.
- [4] I.M. Bodrov, L.O. Apelbaum, M.I. Temkin, *Kinet. Catal.* 5 (1964) 696–705.
- [5] A.A. Khomenko, L.O. Apelbaum, F.S. Schub, Y.S. Snagovskii, M.I. Temkin, *Kinet. Catal.* 12 (1971) 423–430.
- [6] Y.S. Snagovskii, A.A. Khomenko, R.A. Ivanova, F.S. Schub, M.I. Temkin, *Kinet. Catal.* 19 (1978) 942–949.
- [7] I.M. Bodrov, L.O. Apelbaum, M.I. Temkin, *Kinet. Catal.* 9 (1968) 1065–1071.
- [8] J.R.H. Ross, M.C.F. Steel, *J. Chem. Soc. Faraday Trans. 1* 69 (1973) 10–20.
- [9] J. Wei, E. Iglesia, *J. Catal.* 224 (2004) 370–383.
- [10] J.C. De Deken, E.F. Devos, G.F. Froment, *Steam Reforming of Natural Gas: Intrinsic Kinetics, Diffusional Influences, and Reactor Design*, chap. vol. 17, 1982, pp. 181–197.
- [11] J. Xu, G.F. Froment, *AIChE* 35 (1989) 88–96.
- [12] K. Hou, R. Hughes, *Chem. Eng. J.* 82 (2001) 311–328.
- [13] A.K. Avetisov, J.R. Rostrup-Nielsen, V.L. Kuchaev, J. Bak Hansen, A.G. Zyskin, E.N. Shapatina, *J. Mol. Catal. A: Chem.* 315 (2010) 155–162.
- [14] S.S.E.H. Elnashaie, A.M. Adris, A.S. Al-Ubaid, M.A. Soliman, *Chem. Eng. Sci.* 45 (1990) 491–501.
- [15] I.M. Bodrov, L.O. Apelbaum, M.I. Temkin, *Kinet. Catal.* 8 (1967) 821–828.
- [16] D.W. Allen, E.R. Gerhard, M.R. Likins Jr., *Ind. Eng. Chem. Process Des. Dev.* 14 (1975) 256–259.
- [17] O. Dewaele, G.F. Froment, *J. Catal.* 184 (1999) 499–513.
- [18] T. Osaki, T. Horiuchi, K. Suzuki, T. Mori, *J. Chem. Soc. Faraday Trans. 92* (1996) 1627–1631.
- [19] N.W. Cant, R. Dümpekmann, A.M. Maitra, *Stud. Surf. Sci. Catal.* 107 (1997) 491–496.
- [20] L.M. Aparicio, *J. Catal.* 165 (1997) 262–274.
- [21] D. Chen, R. Lødeng, K. Omdahl, A. Anundskås, O. Olsvik, A. Holmen, *Stud. Surf. Sci. Catal.* 139 (2001) 93–100.
- [22] D. Chen, R. Lødeng, A. Anundskås, O. Olsvik, A. Holmen, *Chem. Eng. Sci.* 56 (2001) 1371–1379.
- [23] L. Maier, B. Schädel, K. Herrera Delgado, S. Tischer, O. Deutschmann, *Top. Catal.* 54 (2011) 845–863.
- [24] D.W. Blaylock, T. Ogura, W.H. Green, G.J.O. Beran, *J. Phys. Chem. C* 113 (2009) 4898–4908.
- [25] H.S. Bengaard, J.K. Nørskov, J. Sehested, B.S. Clausen, L.P. Nielsen, A.M. Molenbroek, J.R. Rostrup-Nielsen, *J. Catal.* 209 (2002) 365–384.
- [26] D. Chen, R. Lødeng, H. Svendsen, A. Holmen, *Ind. Eng. Chem. Res.* 50 (2011) 2600–2612.
- [27] G. Jones, J.G. Jakobsen, S.S. Shim, J. Kleis, M.P. Andersson, J. Rossmeisl, F. Abild-Pedersen, T. Bligaard, S. Helveg, B. Hinnemann, J.R. Rostrup-Nielsen, I. Chorkendorff, J. Sehested, J.K. Nørskov, *J. Catal.* 259 (2008) 147–160.
- [28] D.W. Blaylock, Y.-A. Zhu, W.H. Green, *Top. Catal.* 54 (2011) 828–844.
- [29] C. Sprung, B. Arstad, U. Olsbye, *ChemCatChem* 6 (2014) 1969–1982.
- [30] C. Sprung, B. Arstad, U. Olsbye, *Top. Catal.* 54 (2011) 1063–1069.
- [31] M. Wolfsberg, W.A. Van Hook, P. Paneth, L.P.N. Rebelo, *Isotope Effects*, Springer, Dordrecht, 2010.
- [32] E.V. Anslyn, D.A. Dougherty, *Modern Physical Organic Chemistry*, University Science Books, Sausalito, CA, 2006.
- [33] H.C. Urey, D. Rittenberg, *J. Chem. Phys.* 1 (1933) 137–143.
- [34] S.L. Kiperman, *Theor. Exp. Chem.* 12 (1976) 8–11.
- [35] C. Sprung, *Kinetic Investigation in Methane Steam Reforming Over a Nickel Catalyst*, University of Oslo, Norway, 2012 (Ph.D. thesis).
- [36] K. Metaxas, J.W. Thybaut, G. Morra, D. Farrusseng, C. Mirodatos, G.B. Marin, *Top. Catal.* 53 (2010) 64–76.
- [37] P.N. Brown, A.C. Hindmarsh, L.R. Petzold, *SIAM J. Sci. Comput.* 15 (1994) 1467–1488.
- [38] <http://www.netlib.org/>, (accessed 13.03.11).
- [39] H.H. Rosenbrock, *Comput. J.* 3 (1960) 175–184.
- [40] D.W. Marquardt, *J. Soc. Ind. Appl. Math.* 3 (1963) 431–441.
- [41] P.T. Boggs, J.R. Donaldson, R.H. Byrd, R.B. Schnabel, *ACM Trans. Math. Softw.* 15 (1989) 348–364.
- [42] D.M. Himmelblau, *Process Analysis by Statistical Methods*, John Wiley & Sons, Inc., New York, 1970.
- [43] M.C.J. Bradford, M.A. Vannice, *Appl. Catal. A* 142 (1996) 97–122.
- [44] T. Mori, H. Masuda, H. Imai, A. Miyamoto, S. Baba, Y. Murakami, *Chem. Lett.* 10 (1981) 831–834.
- [45] M. Agnelli, H.M. Swaan, C. Marquez-Alvarez, G.A. Martin, C. Mirodatos, *J. Catal.* 175 (1998) 117–128.
- [46] T. Mori, H. Masuda, H. Imai, A. Miyamoto, S. Baba, Y. Murakami, *J. Phys. Chem.* 86 (1982) 2753–2760.
- [47] Z.A. Ibraeva, V.N. Nekrasov, V.I. Yakerson, B.S. Gudkov, E.Z. Golosman, Z.T. Beisembaeva, S.L. Kiperman, *Kinet. Catal.* 28 (1987) 386–391.
- [48] B. Shi, C. Jin, *Appl. Catal. A* 393 (2011) 178–183.
- [49] J.A. Dumesic, D.F. Rudd, L.M. Aparicio, J.E. Rekoske, A.A. Treviño, *The Microkinetics of Heterogeneous Catalysis*, Wiley-VCH, 1993.
- [50] A. Roine, HSC Chemistry® 5.11 for Windows, Outokumpu Research Oy, FIN-28101 PORI, 2002 <http://www.hsc-chemistry.net/>
- [51] M.A. Soliman, A.M. Adris, A.S. Al-Ubaid, S.S.E. El-Nashaie, *J. Chem. Technol. Biotechnol.* 55 (1992) 131–138.
- [52] M. Maestri, D.G. Vlachos, A. Beretta, G. Groppi, E. Tronconi, *J. Catal.* 259 (2008) 211–222.
- [53] A.D. Karmazyn, V. Fiorin, S.J. Jenkins, D.A. King, *Surf. Sci.* 538 (2003) 171–183.
- [54] B.E. Spiewak, J.A. Dumesic, *Thermochim. Acta* 290 (1997) 43–53.
- [55] N. Al-Sarraf, D.A. King, *Surf. Sci.* 307–309 (1994) 1–7.
- [56] N. Al-Sarraf, J.T. Stuckless, C.E. Wartnaby, D.A. King, *Surf. Sci.* 283 (1993) 427–437.

- [57] K. Christmann, O. Schober, G. Ertl, M. Neumann, J. Chem. Phys. 60 (1974) 4528–4540.
- [58] F.J. Bröcker, G. Wedler, Discuss. Faraday Soc. 41 (1966) 87–94.
- [59] G. Wedler, F.J. Bröcker, Surf. Sci. 26 (1971) 454–460.
- [60] A.C. Zettlemoyer, J.J. Chessick, J. Phys. Chem. 58 (1954) 242–245.
- [61] O. Beeck, Adv. Catal. 2 (1950) 151–195.
- [62] G.D. Sakumbaeva, S.V. Artamonov, S.T. Omarov, Kinet. Catal. 23 (1982) 713–717.
- [63] J. Lapujoulade, K.S. Neil, Surf. Sci. 35 (1973) 288–301.
- [64] E. Shustorovich, Metal-Surface Reaction Energetics, vol. 1, VCH Publishers Inc., 1991.
- [65] W.W. Akers, D.P. Camp, AIChE 1 (1955) 471–475.
- [66] R. Köpsel, Freiburger Forschungshefte A 672 (1983) 58–79.